

Supplemental Information: Design Principles from Glass Sponges for Structurally Robust Lattices

MATHEUS C. FERNANDES¹, JAMES C. WEAVER², JOANNA AIZENBERG^{1,2,3}, AND KATIA BERTOLDI^{1,2,3,*}

¹ John A. Paulson School of Engineering and Applied Sciences – Harvard University, Cambridge, MA 02138

² Wyss Institute – Harvard University, Cambridge, MA 02138

³ Kavli Institute – Harvard University, Cambridge, MA 02138

* Corresponding author: bertoldi@seas.harvard.edu

Compiled December 7, 2018

¹ S1. STRUCTURE OF THE HEXACTINELLID SPONGE *EUPLECTELLA ASPERGILLUM*

² The periodic structures investigated in this study are inspired by the skeleton of the Hexactinellid sponge *Euplectella aspergillum* (sp.), commonly known as the "Venus' flower basket". In this section we provide a detailed description of the sponge geometry and measured dimensions.

⁵ Figure S1 shows a photograph of the entire skeleton of the *Euplectella* sp., and its intricate, cylindrical cage-like structure (20 to 25cm long, 2 to 4 cm in diameter)^[1]. The surface of the cylinder consists of a regular square lattice composed of a series of cemented vertical and horizontal struts with circular cross-section. The cell spacing between horizontal and vertical struts was reported to be $L \approx 2.5\text{mm}$ ^[2], while their diameter was measured to be $D_{nd} \approx 0.25\text{mm}$ ^[2]. Besides the horizontal and vertical struts, there is an additional set of diagonal elements, intersecting in a manner that creates a series of alternating open and closed cells, reminiscent of a checkerboard pattern^[2]. Although these diagonal elements are not as ordered as the horizontal and vertical ones, it has been shown that they can be approximated with two diagonal struts that are offset from the nodes (vertex joints between non-diagonal elements) and form octagonal openings (fig. S1(d)). To estimate the volume ratio between diagonal and non-diagonal elements, we took high resolution photographs of the sponge and performed image segmentation to segregate the projected area of the vertical/horizontal and diagonal spicules. Using this approach, the projected area ratio of non-diagonal to diagonal elements was found to be $A_{nd}/A_d \approx 1.4$. Note that here, and in the following, the subscripts *d* and *nd* are used to indicate diagonal and non-diagonal (i.e. horizontal and vertical) elements, respectively.

¹⁸ Finally, it should also be noted that the sponge is reinforced by external ridges that extend perpendicular to the surface of the cylinder and spiral the cage at an angle of 45°. However, in this paper we do not report the effects of these ridges on its structural performance.

²¹ S1.1. Image Segmentation Analysis

²² →@James, add details of image segmentation analysis performed for extracting diameter ratios between diagonals and non-diagonals

²⁴ S2. OUR FOUR DESIGNS

²⁵ In this study, we focus on four different lattice configurations (Designs A, B, C and D) constrained to deform in an in-plane setting only. In an effort to conduct a fair performance comparison between the different designs, all four designs are characterized by the same total volume of material and a fixed volume ratio between non-diagonal and diagonal elements (chosen to match the sponge geometry). Two different shapes are considered for the cross-section of the struts: circular and rectangular. For the circular cross-section case we denote the diameters with $D_{\alpha,nd}$ and $D_{\alpha,d}$ of the non-diagonal (i.e. horizontal and vertical) and diagonal struts in the α -th design, respectively, and neglect out-of-plane buckling. For the rectangular cross-sections we choose the depth H and in-plane thickness $T_{\alpha,nd}$ and $T_{\alpha,d}$ to avoid out-of-plane deformation (i.e. we choose the depth over thickness ratio sufficiently large). Finally, it is important to note that the slenderness of the non-diagonal members in the α -th design $\in [A, B, C]$ is chosen as

$$\frac{D_{\alpha,nd}}{L} = 0.1, \quad \text{and} \quad \frac{T_{\alpha,nd}}{L} = 0.1, \quad (\text{S1})$$

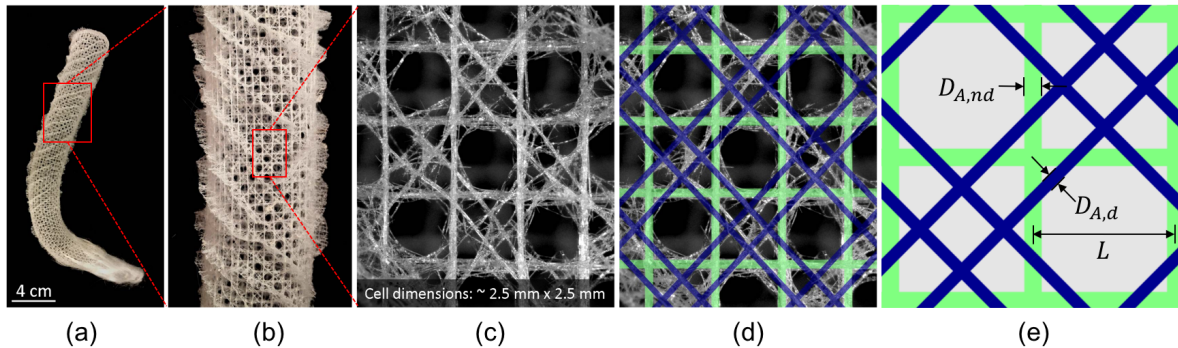


Figure S1: Hexactinellid sponge *Euplectella aspergillum*. (a)-(b) Full-frame photo of sponge. (c) Close up microscope image of the sponge. (d) Comparison between the idealized model (green and blue lines) and the sponge structure. (e) Unit cell of the idealized model.

34 for the case of circular and rectangular cross section, since this is the aspect ratio measured for the sponges (see [section S1](#)).
 35 In the subsequent sections, we describe in detail the unit cells for four different designs, and provide the derivations
 36 for each geometry cross-section characteristics.

37 S2.1. Design A

38 Design A is inspired by the sponge structure and consists of a square grid reinforced by a double diagonal system
 39 (see [fig. S2](#)). As for the case of the sponge, the diagonal elements are assumed to form an octagonal opening on every
 40 other cell, so that they intersect the horizontal and vertical struts at a distance $\Delta L = L/(\sqrt{2} + 2)$ from the nodes, where L
 41 denote the length of the vertical/horizontal struts.

42 S2.1.1. Circular cross section

43 If we assume that cross section of all struts is circular, the projected area and volume for the non-diagonal ($A_{A,nd}$ and
 44 $V_{A,nd}$) and diagonal ($A_{A,d}$ and $V_{A,d}$) members is given by

$$45 \quad A_{A,nd} = 8LD_{A,nd}, \quad (S2)$$

$$46 \quad V_{A,nd} = 8L \left(\pi \frac{D_{A,nd}^2}{4} \right) = 2L\pi D_{A,nd}^2 \quad (S3)$$

$$47 \quad A_{A,d} = 8\sqrt{2}LD_{A,d}, \quad (S4)$$

48 and

$$49 \quad V_{A,d} = 8\sqrt{2}L \left(\pi \frac{D_{A,d}^2}{4} \right) = 2\sqrt{2}L\pi D_{A,d}^2. \quad (S5)$$

50 Since the projected area ratio of the non-diagonal to diagonal elements in the sponge has been measured to be

$$51 \quad \frac{A_{A,nd}}{A_{A,d}} = 1.4, \quad (S6)$$

52 by substituting [eq. \(S2\)](#) and [eq. \(S4\)](#) into the equation above we find that for Design A

$$53 \quad D_{A,nd} = 1.4\sqrt{2}D_{A,d} \approx 2D_{A,d}. \quad (S7)$$

54 Substitution of [eq. \(S7\)](#) into [eq. \(S3\)](#) and [eq. \(S5\)](#) yields

$$55 \quad \frac{V_{A,nd}}{V_{A,d}} = \frac{2L\pi D_{A,nd}^2}{2\sqrt{2}L\pi D_{A,d}^2} = 2\sqrt{2} \quad (S8)$$

56 and

$$57 \quad V_{A,T} = V_{A,nd} + V_{A,d} = 2\pi L(D_{A,nd}^2 + \sqrt{2}D_{A,d}^2) = 2\pi LD_{A,nd}^2 \left(1 + \frac{1}{2\sqrt{2}} \right), \quad (S9)$$

52 where $V_{A,T}$ indicates the total volume of the unit cell for Design A.

53 Finally, it is important to note that in this study we use Design A as our base model, and thus constrain the total
54 volume of all the other unit cell designs with circular cross section to be equal to that of Design A, namely,

$$V_{\alpha,d} + V_{\alpha,nd} = V_{A,T} = 2\pi LD_{A,nd}^2 \left(1 + \frac{1}{2\sqrt{2}}\right), \quad (\text{S10})$$

55 with $\alpha = B, C$ and D. For Designs B and C, which comprise diagonal elements, we also constrain the volume ratio of the
56 non-diagonal to diagonal elements to be the same as in Design A

$$\frac{V_{\alpha,nd}}{V_{\alpha,d}} = \frac{V_{A,nd}}{V_{A,d}} = 2\sqrt{2}, \quad (\text{S11})$$

57 with $\alpha \in B$ and C.

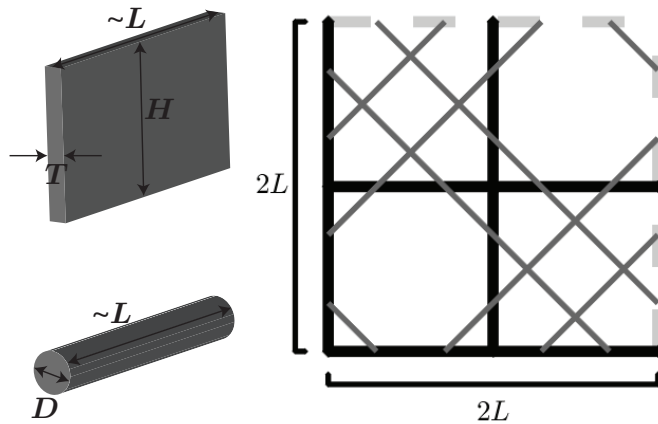


Figure S2: Unit cell for Design A. This design is inspired by the sponge structure and consists of a square grid reinforced by a double diagonal system. The horizontal and vertical struts have length L and circular cross section with diameter $D_{A,nd}$ and, as with the sponge, we assume $D_{A,nd}/L = 0.1$. The diagonal elements have a circular cross section with diameter $D_{A,d} = 2D_{A,nd}$.

58 S2.1.2. Rectangular cross-section

59 If we assume that the cross section of all struts is rectangular, the projected-area for the non-diagonal ($A_{A,nd}$) and
60 diagonal ($A_{A,d}$) members is given by

$$A_{A,nd} = 8LT_{A,nd} \quad (\text{S12})$$

61 and

$$A_{A,d} = 8\sqrt{2}LT_{A,d} \quad (\text{S13})$$

62 where $T_{A,nd}$ and $T_{A,d}$ are the non-diagonal and diagonal in-plane strut thickness for Design A, respectively. Since for the
63 sponge $A_{nd}/A_d \approx 1.4$, it follows that

$$T_{A,nd} = 2T_{A,d}. \quad (\text{S14})$$

64 Finally, also for the case of rectangular cross-section we use Design A as our base model, and thus constrain the total
65 volume of all the other unit cell designs with rectangular cross-section to be equal to that of Design A, namely,

$$V_{A,T} = V_{\alpha,d} + V_{\alpha,nd} = 8LH(T_{A,nd} + \sqrt{2}T_{A,d}) = 8LHT_{A,nd} \left(1 + \frac{1}{\sqrt{2}}\right), \quad (\text{S15})$$

66 with $\alpha \in B, C$ and D. Moreover, for Designs B and C, which comprise diagonal elements, we also constrain the volume
67 ratio of the non-diagonal to diagonal elements to be the same as in Design A,

$$\frac{V_{\alpha,nd}}{V_{\alpha,d}} = \sqrt{2}, \quad (\text{S16})$$

68 with $\alpha \in B$ and C.

69 S2.2. Design B

70 Design B is similar to the sponge design (Design A) and is likewise characterized by an alternation of open and closed 71 cells (fig. S3). However, instead of having two diagonals offset from the nodes, here we only have one diagonal passing 72 through the nodes and crossing every other cell.

73 S2.2.1. Circular cross section

74 For this design with circular cross section the non-diagonal and diagonal volumes are given by

$$V_{B,nd} = V_{A,nd} = 2\pi LD_{B,nd}^2 \quad (\text{S17})$$

75 and

$$V_{B,d} = 2\sqrt{8}L \left(\pi \frac{D_{B,d}^2}{4} \right), \quad (\text{S18})$$

76 respectively. Using the constraints provided by eq. (S10) and eq. (S11), as well as the above volumes, we obtain

$$D_{B,nd} = D_{A,nd} \quad (\text{S19})$$

77 and

$$\frac{D_{B,d}}{D_{B,nd}} = \frac{1}{\sqrt{2}}. \quad (\text{S20})$$

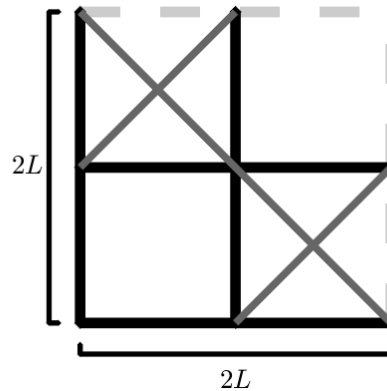


Figure S3: Unit cell for Design B. This design is still characterized by an alternation of open and closed cells. However, instead of having two diagonals offset from the nodes, here we only have one diagonal passing through the nodes and crossing every other cell. The horizontal and vertical struts have length L and a circular cross section with diameter $D_{B,nd}$. The diagonal elements have a circular cross section with diameter $D_{B,d} = D_{B,nd}/\sqrt{2}$.

78 S2.2.2. Rectangular cross section

79 For this design with circular cross section the volume of the non-diagonal and diagonal members are given by

$$V_{B,nd} = 8LT_{B,nd}H. \quad (\text{S21})$$

80 and

$$V_{B,d} = 4\sqrt{2}LT_{B,d}H. \quad (\text{S22})$$

81 Using the constraints provided by eq. (S15) and eq. (S16), as well as the above volumes, we obtain

$$T_{B,nd} = T_{B,d} \quad (\text{S23})$$

82 and

$$T_{B,nd} = T_{A,nd} \quad (\text{S24})$$

83 S2.3. Design C

84 Design C is inspired by the town lattice truss design introduced by architect Ithiel Town in 1820^[3] and consists of 85 every cell being reinforced by diagonal trusses passing through the nodes (see fig. S4).

86 S2.3.1. Circular cross section

87 For this design with circular cross section, the volume of the non-diagonal and diagonal members of the unit cell are
 88 given by:

$$V_{C,nd} = V_{A,nd} = 2L\pi D_{A,nd}^2 \quad (\text{S25})$$

89 and

$$V_{C,d} = V_{A,d} = 2\sqrt{2}L\pi D_{A,d}^2, \quad (\text{S26})$$

90 respectively. Using the constraints provided by eq. (S10) and eq. (S11) we obtain

$$D_{C,nd} = D_{A,nd} \quad (\text{S27})$$

91 and

$$\frac{D_{C,d}}{D_{C,nd}} = \frac{1}{2}. \quad (\text{S28})$$

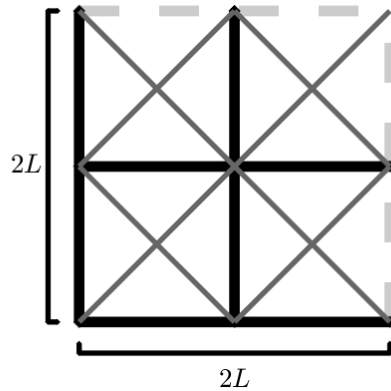


Figure S4: Unit cell for Design C. This design consists of a square grid with all cells being reinforced by diagonal trusses passing through the nodes. The horizontal and vertical struts have length L and a circular cross section with diameter $D_{C,nd}$. The diagonal elements have a circular cross section with diameter $D_{C,d} = D_{C,nd}/2$.

92 S2.3.2. Rectangular cross section

93 For this design with circular cross section, the volume of the non-diagonal and diagonal members of the unit cell are
 94 given by

$$V_{C,nd} = 8LT_{C,nd}H \quad (\text{S29})$$

95 and

$$V_{C,d} = 8\sqrt{2}LT_{C,d}H \quad (\text{S30})$$

96 Using the constraints provided by eq. (S15) and eq. (S16), as well as the above volumes, we obtain

$$T_{C,nd} = 2T_{C,d}, \quad (\text{S31})$$

97 and

$$T_{C,nd} = T_{A,nd}. \quad (\text{S32})$$

98 S2.4. Design D

99 Design D comprises only the square grid without diagonal reinforcement (fig. S5). As such, for this design we allocate
 100 the total material volume to the non-diagonal elements. Note that this design is well known to be unstable and very
 101 limited in resisting shear forces^[4,5].

102 S2.4.1. Circular cross section

103 Since

$$V_{D,T} = V_{D,nd} = V_{A,nd} = 2\pi LD_{D,nd}^2, \quad (\text{S33})$$

104 using the constraint provided by eq. (S10) we obtain

$$D_{D,nd} = D_{A,nd} \sqrt{1 + \frac{\sqrt{2}}{4}}. \quad (\text{S34})$$

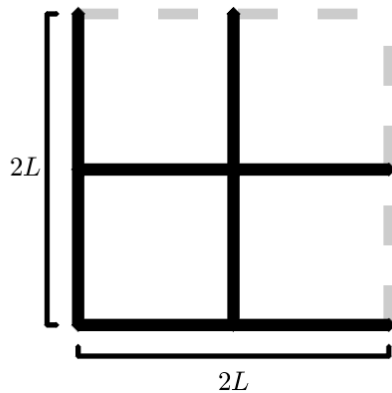


Figure S5: Unit cell for Design D. This design consists of a square grid without diagonal reinforcement. The horizontal and vertical struts have length L and a circular cross section with diameter $D_{D,nd}$.

105 S2.4.2. Rectangular cross-section

106 Since

$$V_{D,T} = V_{D,nd} = 8LT_{D,nd}H, \quad (\text{S35})$$

107 using the constraint provided by eq. (S15) we obtain

$$T_{D,nd} = \left(1 + \frac{1}{\sqrt{2}}\right) T_{A,nd} \quad (\text{S36})$$

108 S3. NUMERICAL MODEL

109 The finite element analysis presented in this article were conducted using the ABAQUS/Standard. All models were
110 constructed using 1D Timoshenko beam (ABAQUS element type B22) and all beam crossings were assumed to be welded
111 joints. For each instance, seeding of the mesh was chosen to be at least 1/10 of the minimum beam length. The response
112 of the material was captured using a linear elastic model with Poisson's ratio $\nu = 0.3$ and Young's modulus of E .

113 To reduce the computational cost, we took advantage of the periodicity of the structures and investigated their
114 response using the unit cells shown in fig. S6. To subject the unit cells to a macroscopic deformation gradient $\bar{\mathbf{F}}$ periodic
115 boundary conditions are imposed on all cell boundaries by enforcing^[6,7]

$$\mathbf{u}_\alpha^{A_i} - \mathbf{u}_\alpha^{B_i} = (\bar{\mathbf{F}}_{\alpha\beta} - \delta_{\alpha\beta})(\mathbf{X}_\beta^{A_i} - \mathbf{X}_\beta^{B_i}), \quad i = 1, 2, \dots, K \quad (\text{S37})$$

116 where $\delta_{\alpha\beta}$ is the Kronecker delta, $\mathbf{u}_\alpha^{A_i}$ and $\mathbf{u}_\alpha^{B_i}$ ($\alpha = 1, 2$) are displacements of points periodically located on the boundary
117 of the unit cell. Moreover, K denotes the number of pairs of nodes periodically located on the boundary of the unit
118 cell. Note that the components of $\bar{\mathbf{F}}$ can be conveniently prescribed within the finite element framework using a set
119 of virtual nodes. The corresponding macroscopic first Piola-Kirchoff stress $\bar{\mathbf{P}}$ is then obtained through virtual work
120 considerations^[6,7].

121 To subject the structures to uniaxial compression, in this study the following uniaxial macroscopic loading condition
122 was considered:

$$\bar{\mathbf{F}} = \begin{bmatrix} \text{UNSET} & 0 \\ 0 & \lambda_y \end{bmatrix} \quad (\text{S38})$$

123 In order to investigate the structure's buckling and elastic stiffness response in all directions, we rotate the unit cell
124 model by angle θ and re-apply the above periodic boundary conditions using the rotated geometry coordinates. This
125 approach allows us to rotate the base orthogonal coordinate system with respect to the unit cell.

126 To determine the initial stiffness of the structures we performed a linear elastic analysis. To calculate stiffness we use a
127 displacement controlled simulation and extract the total reaction force from the model. To obtain the structures response
128 to varying angle, we follow the simple procedure detailed in the previous paragraph to rotate the boundary condition.
129 Knowing the displacement applied and the total reaction force, we can use this information to compute the structural
130 stiffness.

131 For all buckling analysis, we performed a linear stability buckling analysis (*Buckling command in ABAQUS input
132 file). We perform this analysis for varying angles θ and extract the first mode critical buckling strain. Since buckling
133 may alter the periodicity of the structure, we considered super cells consisting of $M \times M$ undeformed RVEs subjected to

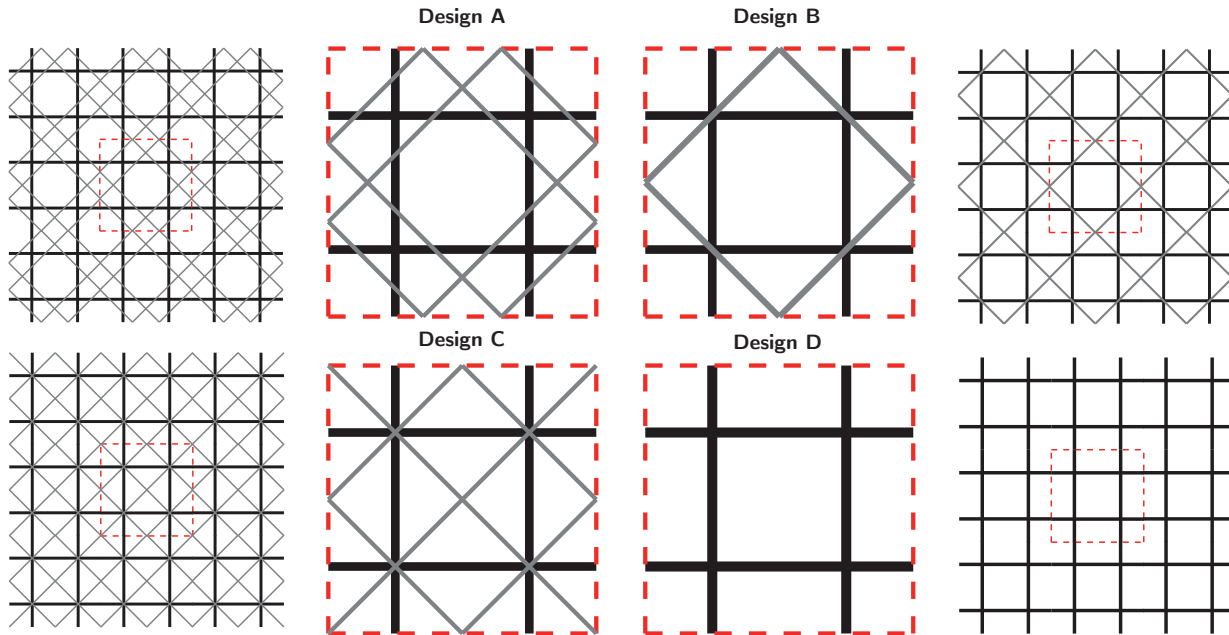


Figure S6: RVE used for the different designs. This figure portrays the different RVEs used for the different designs considered. Each unit cell is shifted by half of a square cell to the horizontally and half of a square cell vertically. Periodic boundary conditions are applied on the nodes that intersect with the light gray dashed line.

134 periodic boundary conditions and calculated the critical strain for each of them. The critical strain of the infinite periodic
 135 structure is then defined as the minimum critical strain on all considered super cells. See fig. S12 for this detailed analysis.
 136 From the main article figure## [→add reference to main article results figure](#) we conclude that for all θ , Design
 137 A provides a higher overall buckling strength over the other compared designs, while not compromising its overall
 138 stiffness in every direction.

139 S4. EXPERIMENTAL SETUP

140 [→add full description of experimental setup and full table of 3D printed material properties; @James: I need to material](#)
 141 [properties](#)

142 S5. OPTIMIZATION ANALYSIS

143 In an effort to identify lattice configurations resulting in large critical loads, we used a Python implementation of the
 144 Covariance Matrix Adaptation Evolution Strategy (CMA-ES)^[8]. CMA-ES is an evolutionary algorithm that is used to
 145 solve optimization/inverse problems by iteratively solving several forward problems to adjust a covariance matrix of
 146 the solution. CMA-ES is a derivative free algorithm, well suited for optimization problems of high dimensionality and
 147 non-linear parameter topology.

148 In this study we used CMA-ES to identify

- 149 • the number of diagonals, N
- 150 • the volume ratio of non-diagonal to diagonal members, $\lambda = V_{nd}/V_d$.
- 151 • the separation between each even set of diagonals, S_i (see Fig. S7)

152 resulting in a lattice structure with the largest critical load. For such optimization problem, the number of optimization
 153 variables increases with the number of diagonals incorporated in the model(i.e. the total number of parameters are
 154 $1 + \frac{1}{2}(N - (N \bmod 2))$ for a given optimization instance with N number of diagonals). Note, for simulations with odd
 155 number of diagonal reinforcements, only an even number of diagonals are separated while keeping one diagonal going
 156 through the non-diagonal junction in order to ensure geometry symmetry (see Fig. S7).

157 The algorithm's initial values are chosen to be in the center of the design space, namely, $\lambda = 1$ and diagonal separation
 158 for the even set of diagonals $S_i = 0.5 * L$. The covariance matrix is initialized uniformly with standard deviation (σ) half
 159 of the domain space, which are normalized to remain between 0 and 1. The optimization is run for uniaxial loading
 160 condition in the direction parallel to the vertical elements.

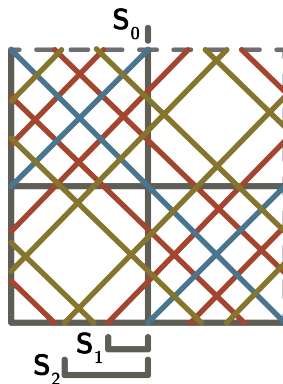


Figure S7: Schematic depicting parameters of Optimization. This schematic shows an example optimization geometry at a complexity level of five diagonals. For each set of even diagonals, we allow each diagonal to travel away from each other from the center junction with distances S_1, S_2 . Note that for every odd diagonal, the distance $S_0 = 0$ and it is not allowed to vary in order to ensure symmetry.

161 For the optimization results presented in the main article, we seek to maximize the critical buckling load using a single
 162 objective target function. However, an equivalent analysis is performed to maximize the critical buckling strain as the
 163 target response (fig. S8.)

	λ	S_1	S_2	S_3	S_4
$N = 1$	3.1454				
$N = 2$	0.5614	0.3390			
$N = 3$	1.4784	0.2440			
$N = 4$	1.0151	0.0989	0.3358		
$N = 5$	0.9509	0.1733	0.3260		
$N = 6$	0.2009	0.2628	0.5827	0.8881	
$N = 7$	0.2962	0.4197	0.6917	0.9126	
$N = 8$	0.3263	0.1553	0.5533	0.7095	0.9113

Table S1: Buckling Load Optimization

	λ	S_1	S_2	S_3	S_4
$N = 1$	0.8908				
$N = 2$	0.4157	0.3233			
$N = 3$	0.3402	0.3268			
$N = 4$	0.2271	0.6103	0.7923		
$N = 5$	0.2772	0.2511	0.4076		
$N = 6$	0.1764	0.2785	0.5743	0.8675	
$N = 7$	0.1810	0.2899	0.5711	0.8443	
$N = 8$	0.1023	0.1459	0.3317	0.5561	0.7843

Table S2: Buckling Strain Optimization

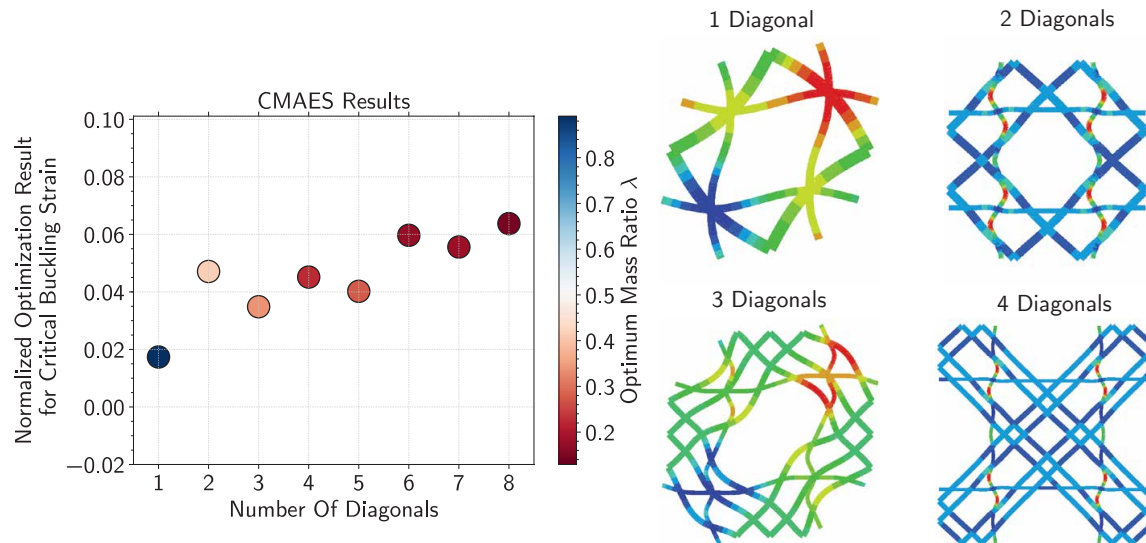


Figure S8: Buckling Optimization. Graph shows optimal value of critical buckling strain for varying number of diagonals. For all simulations, the total mass of the structure is maintained constant while the mass-ratio is allowed to vary. Furthermore, the diagonal separation for each pair of diagonal is allowed to vary together ensuring half symmetry of the structure at all times. The optimization is run under a uniaxial loading condition. The color of each point on the graph corresponds to the optimum value of mass ratio for that particular number of diagonals. Four deformation plots of the optimum structure and buckling modes are provided on the right for their respective number of diagonals.

164 S6. CIRCULAR CROSS-SECTION RESULTS

165 The results presented here complement that found on the main article and show that the structural benefit for the
 166 Design A persists when using a different cross-section for the structure. We show that for varying loading angles all of
 167 the diagonally reinforced designs provide the same stiffness, but Design A consistently provides the best resistance to
 168 buckling.

169 S7. PARAMETER EXPLORATION

170 In order to survey the design space of the double diagonal construction we explore parametric simulations for 2
 171 variables: diagonal separation and mass ratio. For each of these separate analysis, we maintain the sponge geometry as
 172 our base geometry and vary only the respective variable.

173 S7.1. Rectangular Cross Section

174 This section shows the results when using a rectangular cross-section for the truss members. From fig. S10(a) it is
 175 apparent that there exists an optimum for the diagonal separation that occurs when the spacing between diagonals are
 176 approx 0.2 of the horizontal distance between vertical struts. This optimum value also persists when varying the loading
 177 angle. From fig. S10(b) it can be seen that the linear stiffness is symmetrically and almost purely dependent on the mass
 178 ratio allocated to diagonal versus non-diagonal elements. Comparing this figure to fig. S11(b) we can also see that even
 179 the design cross-section does not change the linear stiffness behavior. fig. S10(c) shows that there exists two optimum
 180 mass ratios, one where more material is allocated to the diagonal and one where there is more material allocated to
 181 non-diagonals.

182 S7.2. Circular Cross Section

183 For this cross-section we stay consistent with the natural sponge, and we can see from fig. S11 the overall behavior has
 184 second order differences for (a), no change for (b) and a large difference in relative magnitude for (c). Furthermore, we
 185 can see from the comparison between this section and section S7.1 that by using a rectangular cross-section we can tune
 186 the mass ratio to achieve an overall structure with higher critical buckling strength.

187 S8. LOCAL AND GLOBAL INSTABILITIES

188 How should I go about describing this here?

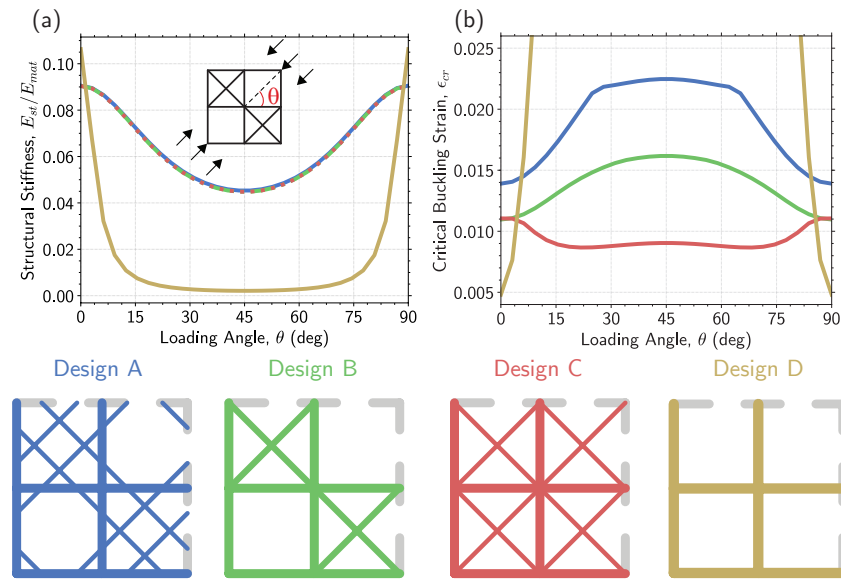


Figure S9: Circular Cross Section Results. The color of the lines correspond to its respective design color below the plots. (a) Shows the linear elastic stiffness of the different designs as a function of the loading angle. All structures except for the design without diagonal reinforcement have the same stiffness. (b) Shows the critical buckling strain for varying loading angle. For all angles, Design A outperforms other diagonally reinforced designs. These results show that the two diagonal benefit persists beyond a particular beam cross-section design.

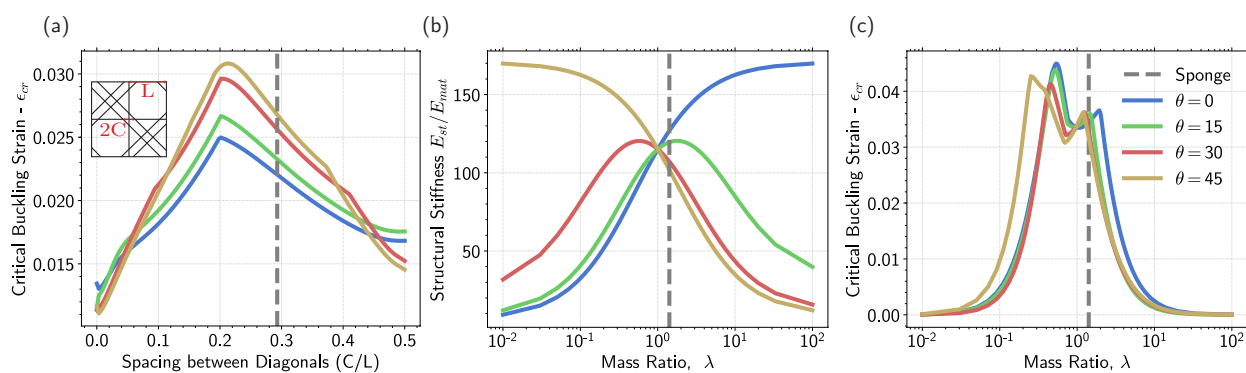


Figure S10: Rectangular Cross Section Parameter Exploration. For each of these plots, we vary a single parameter while maintaining the base sponge inspired geometry constant. The gray line indicates the sponge design parameter. (a) Shows the critical buckling strain for varying spacing between diagonals. (b) Shows the structural stiffness of the geometry as we vary the mass ratio λ . (c) Shows the critical buckling strain of the geometry as we vary the mass ratio λ .

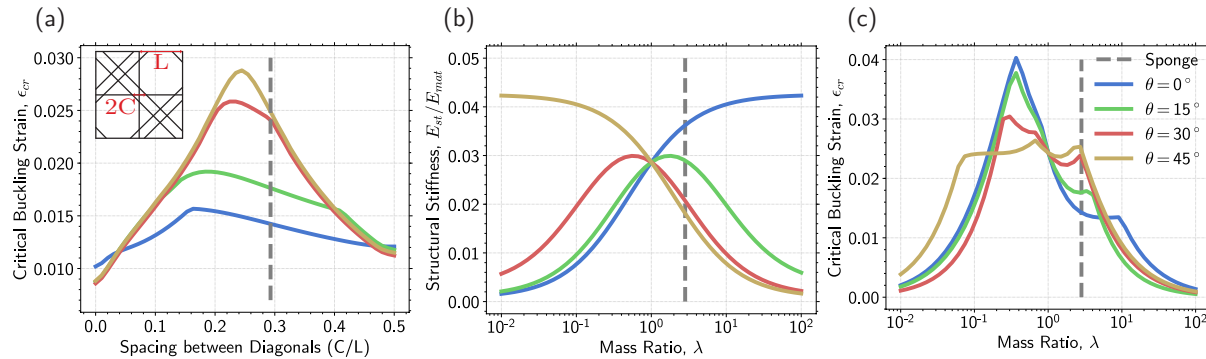


Figure S11: Circular Cross Section Parameter Exploration. For each of these plots, we vary a single parameter while maintaining the base sponge inspired geometry constant. The gray line indicates the sponge design parameter. (a) Shows the critical buckling strain for varying spacing between diagonals. (b) Shows the structural stiffness of the geometry as we vary the mass ratio λ . (c) Shows the critical buckling strain of the geometry as we vary the mass ratio λ .

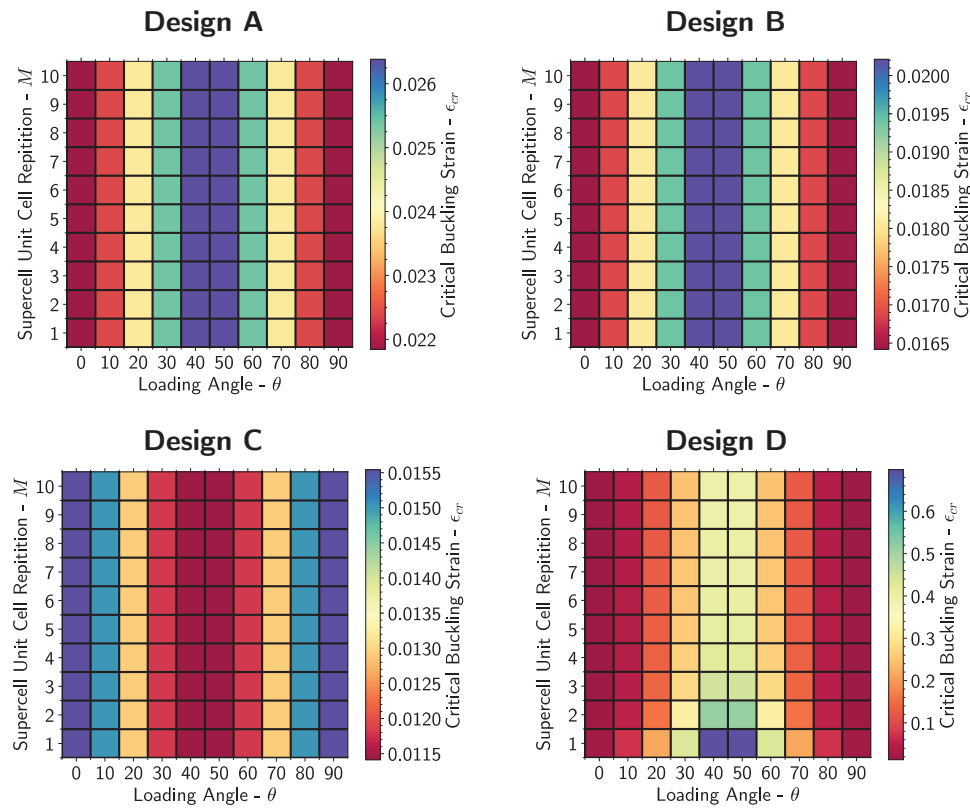
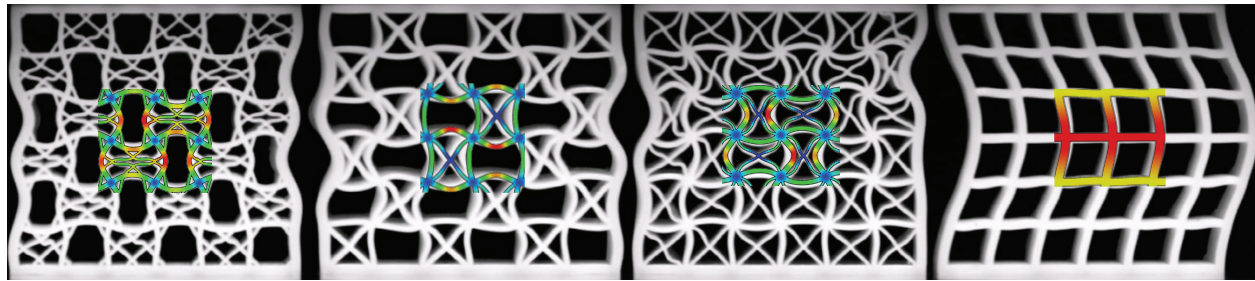
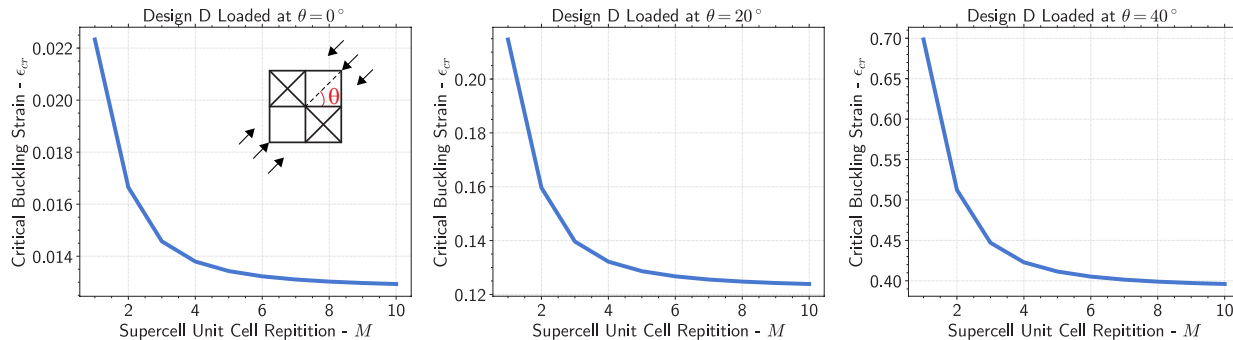


Figure S12: Global vs Local Instabilities. This figure shows four identical analysis performed on the Designs A-D. For each analysis we obtain the critical buckling strain for varying $M \times M$ tessellations (y-axis) of the unit cell also for varying loading angle θ (x-axis). The color of a pixel corresponds to a value of critical buckling strain for that simulation. For each of the simulations, periodic boundary conditions are applied along the outer perimeter of the $M \times M$ structure. This plot conveys that for Designs A-C the prominent buckling mode is the local mode, whereas for Design D, the prominent mode is a global mode. Choosing a sufficiently large M allows Design D to converge to a finite value for each θ .

**Figure S13:** asdf. asdf**Figure S14:** asdf. asdf

189 S9. STRESS CONCENTRATION

190 → add section on stress concentration for plane strain setting

191 REFERENCES

- 192 [1] Joanna Aizenberg, James C Weaver, Monica S Thanawala, Vikram C Sundar, Daniel E Morse, and Peter Fratzl.
193 Skeleton of euptectella sp.: structural hierarchy from the nanoscale to the macroscale. *Science*, 309(5732):275–278,
194 2005.
- 195 [2] James C Weaver, Joanna Aizenberg, Georg E Fantner, David Kisailus, Alexander Woesz, Peter Allen, Kirk Fields,
196 Michael J Porter, Frank W Zok, Paul K Hansma, et al. Hierarchical assembly of the siliceous skeletal lattice of the
197 hexactinellid sponge euptectella aspergillum. *Journal of structural biology*, 158(1):93–106, 2007.
- 198 [3] John Alexander Low Waddell. *Bridge engineering*, volume 1. J. Wiley, 1916.
- 199 [4] Lorna J Gibson and Michael F Ashby. *Cellular solids: structure and properties*. Cambridge university press, 1999.
- 200 [5] VS Deshpande, MF Ashby, and NA Fleck. Foam topology: bending versus stretching dominated architectures. *Acta
201 Materialia*, 49(6):1035–1040, 2001.
- 202 [6] M. Danielsson, D. M. Parks, and M. C. Boyce. Three-dimensional micromechanical modeling of voided polymeric
203 materials. *Journal of Mechanics Physics of Solids*, 50:351–379, February 2002. .
- 204 [7] K. Bertoldi and M. C. Boyce. Mechanically triggered transformations of phononic band gaps in periodic elastomeric
205 structures. *Phys. Rev. B*, 77:052105, Feb 2008. . URL <https://link.aps.org/doi/10.1103/PhysRevB.77.052105>.
- 206 [8] N. Hansen, S. D. Müller, and P. Koumoutsakos. Reducing the time complexity of the derandomized evolution strategy
207 with covariance matrix adaptation (cma-es). *Evolutionary Computation*, 11(1):1–18, March 2003. ISSN 1063-6560. .

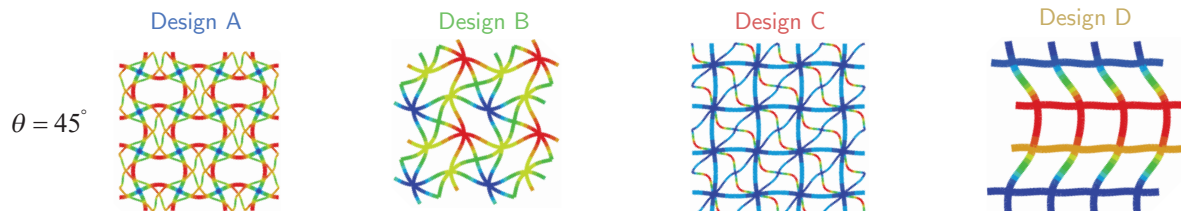


Figure S15: asdf. asdf

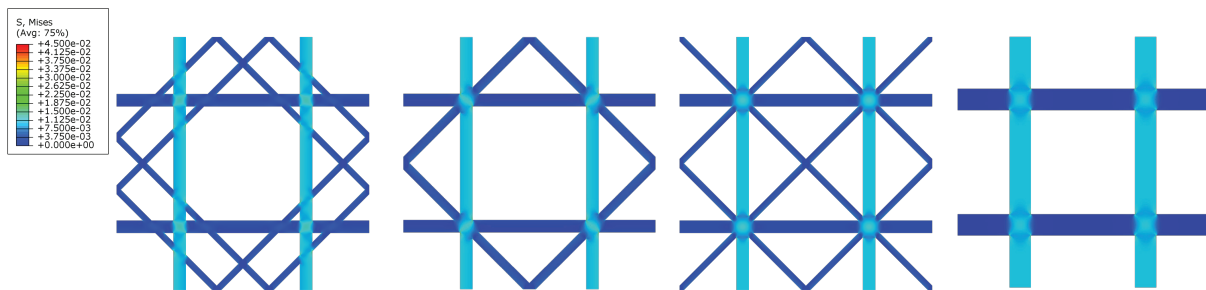


Figure S16: Stress Concentration. Highest Mises Stress for different designs: Design A – 3.362×10^{-2} , Design B – 4.362×10^{-2} , Design C – 4.165×10^{-2} , Design D – 3.550×10^{-2} .

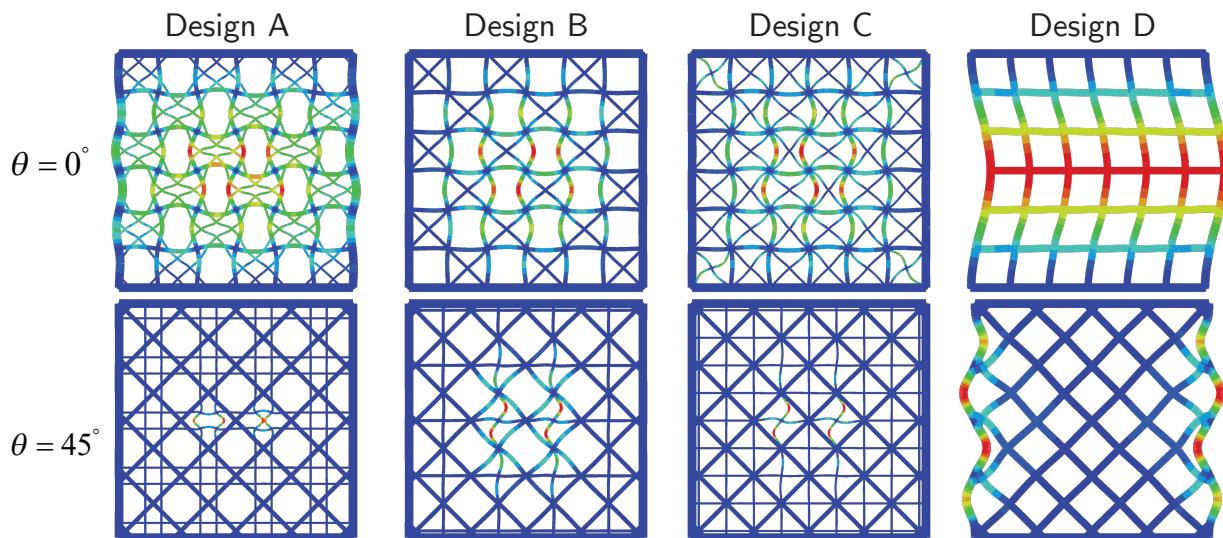


Figure S17: asdf. asdf

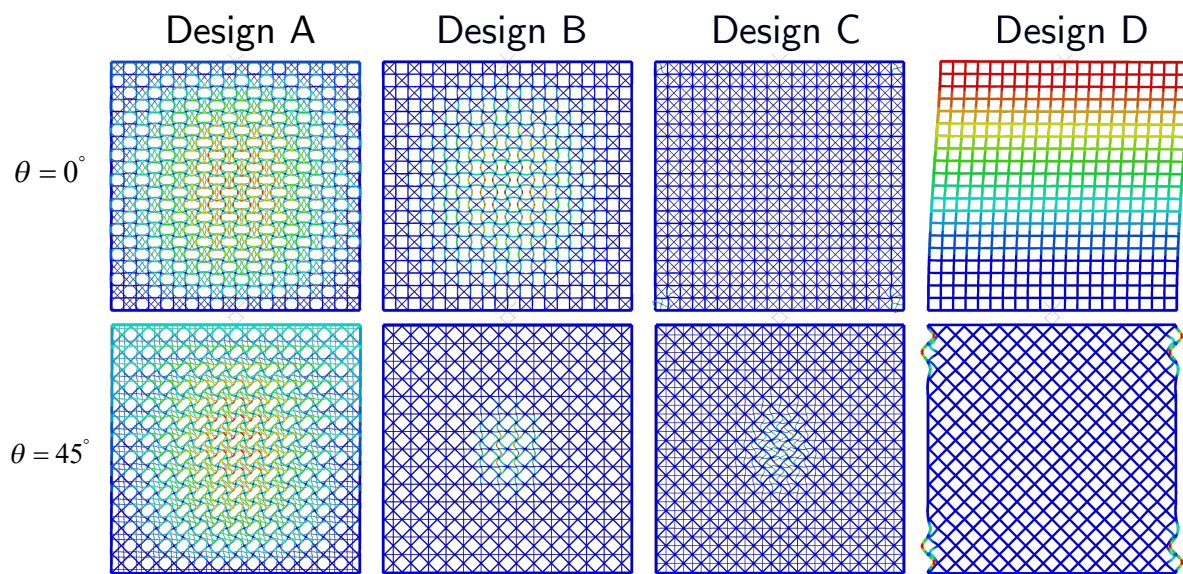
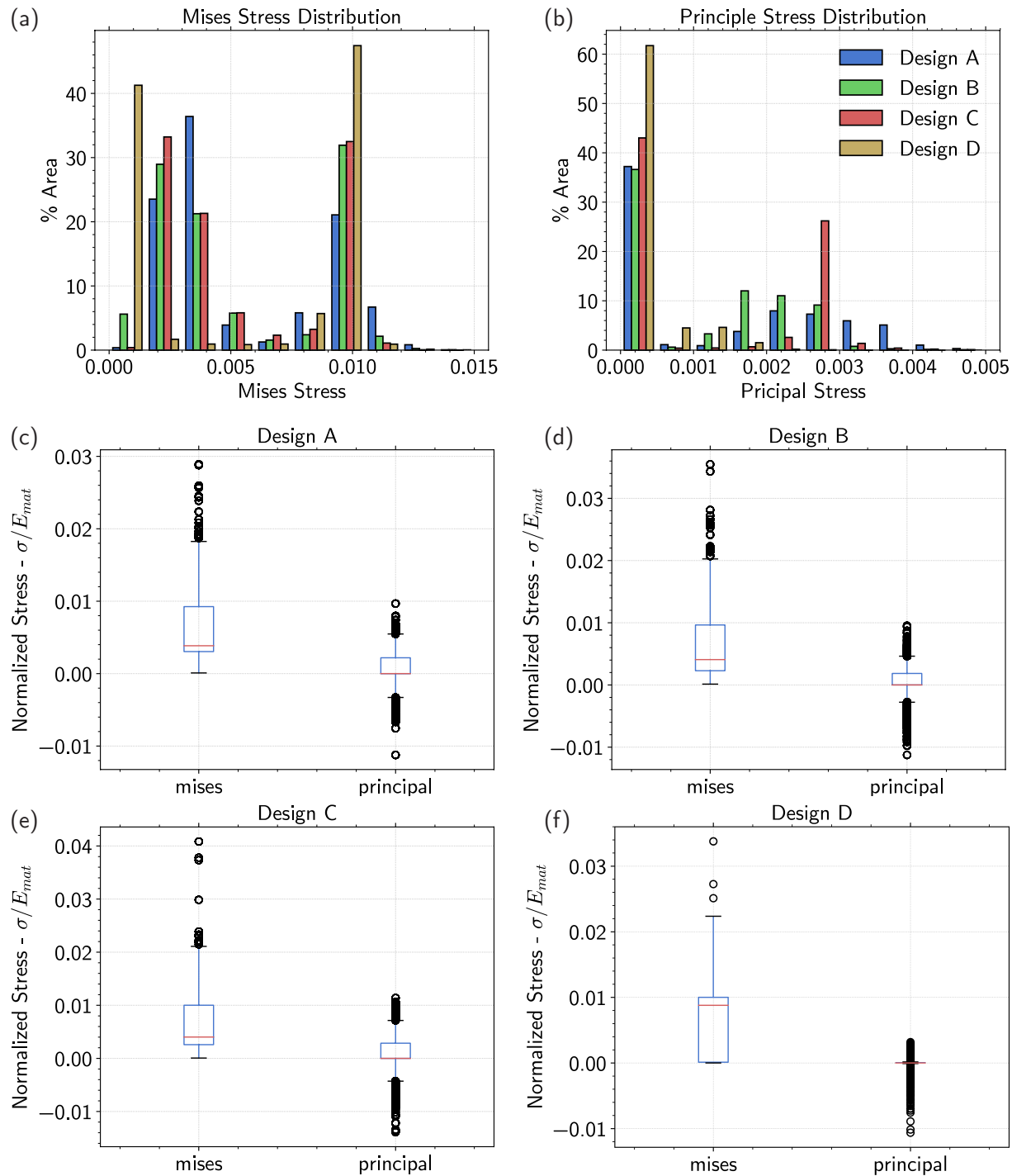


Figure S18: asdf. asdf

**Figure S19:** asdf. asdf

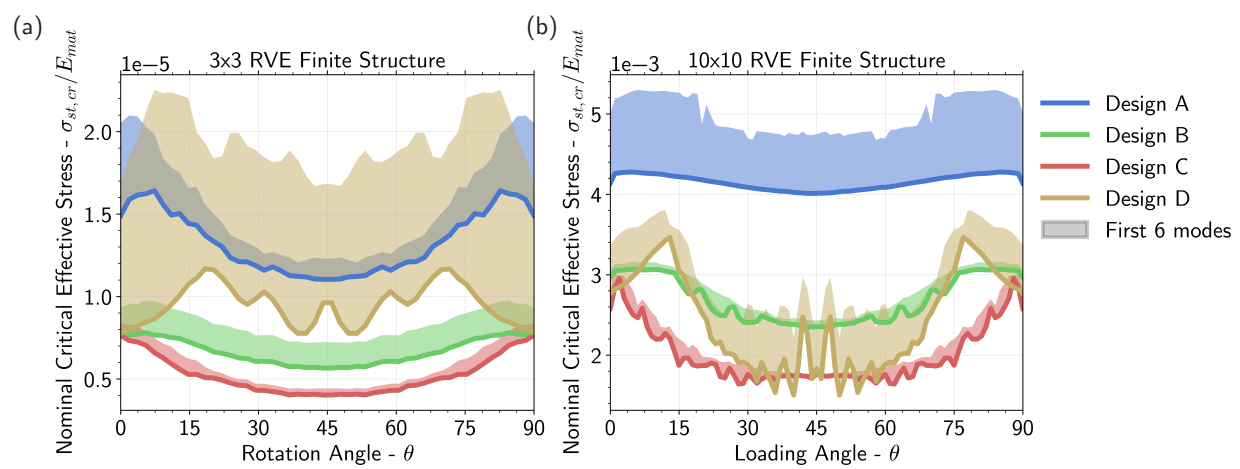


Figure S20: asdf. asdf